Title

Ultrahigh-Capacity Rocksalt Cathodes Enabled by Cycling-Activated Structural Changes

Journal

Advanced Energy Materials, 13(23)

ISSN

1614-6832

Authors

Ahn, Juhyeon

Giovine, Raynald

Wu, Vincent C

et al.

Publication Date

2023-06-01

DOI

10.1002/aenm.202300221

Ultrahigh-Capacity Rocksalt Cathodes Enabled by Cycling-Activated Structural Changes

Juhyeon Ahn, [a] *Raynald Giovine,* [b,c] *Vincent C. Wu,* [b,c] *Krishna Prasad Koirala,* [d,e] *Chongmin Wang,* [d] *Raphaële J. Clément* [b,c] *and Guoying Chen* [a,*]

[a.] *Energy Storage and Distributed Resources Division, Lawrence Berkeley National Laboratory, Berkeley, CA 94720, USA*

[b.] *Materials Department, University of California, Santa Barbara, CA 93106, USA*

[c.] *Materials Research Laboratory, University of California, Santa Barbara, CA 93106, USA*

[d.] *Environmental Molecular Sciences Laboratory, Pacific Northwest National Laboratory, Richland, WA 99354, US*

[e] *Physical and Computational Sciences Directorate, Pacific Northwest National Laboratory, Richland, WA 99354, USA*

[*] *Corresponding author's email:* gchen@lbl.gov

Abstract

Mn-redox based oxides and oxyfluorides are considered most promising as earth-abundant high-energy cathode materials for next-generation lithium-ion batteries. While high capacities are often obtained in high-Mn content cathodes such as Li- and Mn-rich layered and spinel-type oxides and oxyfluorides, local structure changes and structural distortions (particularly those related to layered-to-spinel phase transformations) often lead to voltage fade, capacity decay and impedance rise, resulting in unacceptable electrochemical performance upon cycling. In the present study, we report structural transformations that exploit the high capacity of Mn-rich oxyfluorides while enabling stable cycling, in stark contrast to commonly observed structural changes that result in rapid performance degradation. We show that upon cycling of a cation-disordered rocksalt cathode ($Li_{1.1}Mn_{0.8}Ti_{0.1}O_{1.9}F_{0.1}$, M80), an ultrahigh capacity of ~ 320 mAh/g (energy density of ~ 900 Wh/kg) can be obtained through dynamic structural rearrangements on charge and discharge, along with a unique voltage profile evolution and capacity rise. At high voltage, the presence of Mn^{4+} and Li^+ vacancies promotes local cation ordering, leading to the formation of domains of a so-called "δ phase" within the disordered framework. On deep discharge, Mn^{4+} reduction, along with Li insertion, transform the structure to a partially disordered rocksalt phase with a β'-$LiFeO_2$-type arrangement. At the nanoscale, domains of the *in situ* formed phases are randomly oriented, allowing highly reversible structural changes and stable electrochemical cycling. These new insights not only help explain the superior electrochemical performance of high-Mn DRX, such as M80, but also provide guidance for the future development of Mn-based, high energy density oxide and oxyfluoride cathode materials.

1. Introduction

Mn-rich lithium transition-metal oxides are poised to become the next generation lithium-ion battery (LIB) cathode materials, as they are based on earth-abundant and inexpensive elements.[1-3] For most Mn-based cathodes, maintaining stability is challenging when cycled over a wide voltage window, largely due to local or concerted structural changes during cycling associated with the formation of Jahn-Teller distorted Mn^{3+} ions.[4-6] Some of these changes may be alleviated by increasing cation disorder through defect formation and vacancy sites, as shown in recent studies.[7-9] Furthermore, the overall electrochemical performance of the cathodes, including the voltage profile, capacity, and capacity retention, can be improved by exploring synthesis methods such as mechanochemistry, solid-state and sol-gel synthesis,[10] particle engineering, including size and morphology control,[11-13] as well as compositional modifications by varying the Li and Mn contents, and through cation and anion doping or substitution.[14,15]

Within the chemical space of Li-Mn-O/F, there are a variety of cathode materials exhibiting high capacities (> 250 mAh/g) and reasonable operating voltage windows.[16-19] Their voltage profiles comprise distinct regions, and the potential range and capacity associated with each region are determined by factors such as crystal symmetry, Li and Mn stoichiometries, degree of cation mixing or ordering, as well as crystallographic site occupancy.[8,9,20,21] For example, a typical ordered spinel with a face-centered-cubic anion framework (*e.g.*, $LiMn_2O_4$) has all of its Li in 8a tetrahedral (T_d) sites and Mn in 16d octahedral (O_h) sites (space group, S. G. $Fd\bar{3}m$). This arrangement leads to two characteristic voltage plateaus near 4 V and 3 V *vs*. Li/Li^+ upon cycling.[22] Partial replacement of Mn by Ti in $LiMn_{2-y}Ti_yO_4$ ($1 \leq y < 2$) leads to elongated 4 V and 3 V plateau regions and consequently, increased discharge capacity.[23] Similar electrochemical behavior is observed for the low-temperature (LT) $LiMn_{0.5}Ni_{0.5}O_2$ cathode, which is described as a partially

disordered rocksalt with lithiated-spinel (Li in 16c and Mn in 16d O_h sites, S.G. $Fd\bar{3}m$) and cubic layered (Li in 3a and Mn in 3b O_h sites, S.G. $R\bar{3}m$) local cation arrangements.[24] Oxygen redox is often activated during the first charge process in LT $Li_4Mn_5O_{12}$-like cathodes (similar to a partially disordered Li-rich spinel with Li and Mn in both 8a T_d and 16d O_h, S.G. $Fd\bar{3}m$), which is accompanied by structural rearrangements that lead to a stepped voltage profile on subsequent discharge.[25] A comparable evolution of the voltage profile towards a stepped voltage curve has been observed for ordered structures such as orthorhombic and tetragonal $LiMnO_2$,[26-28] layered Li-deficient and oxygen-rich $Li_{0.7}MnO_{2+z}$ ($0 < z \leq 1$),[29] as well as Li- and Mn-rich layered oxide cathodes containing trivalent Mn.[30] In contrast, it has been found that the 3 V plateau can be circumvented by tuning the Li/Mn and O/F ratios in partially (dis)ordered spinel $Li_{1.4+x}Mn_{1.6}O_{4-z}F_z$ ($0 < x < 1.7$, $0.6 \leq z \leq 0.3$) compounds, where Li and Mn cations reside in the 16c and 16d O_h sites (in addition to Li in 8a T_d sites, S.G. $Fd\bar{3}m$).[31,32]

Mn-based cation-disordered rocksalt (DRX) cathode materials have recently gained intense interest because of their high capacity and energy density, a result of both cationic Mn and anionic O redox participation over a wide voltage window (*e.g.*, 1.5–4.8 V *vs.* Li/Li^+).[33,34] Interestingly, a stepwise voltage profile has also been reported in Li-excess DRX oxides such as $Li_4Mn_2O_5$ and Li_2MnO_3.[35,36] In Mn-rich DRX oxyfluorides, such as the $Li_{1+x}Mn_{0.6+y}Nb_{0.2-y}O_{2-z}F_z$ ($0 < x, y, z \leq 0.2$) compositional series, shallow voltage slopes develop near 4 V and 3 V during cycling,[34] yet the underlying bulk structural changes are not well understood. Detecting subtle changes in the local structure of a long-range disordered compound that appear and disappear during the charge and discharge processes is inherently difficult, however, it is becoming increasingly clear that understanding these dynamic local structural rearrangement is essential to

developing advanced cathode materials, especially those that utilize the intricate space of ordered, disordered, and the intermediate structures in between.

Herein, we successfully synthesized a Mn-enriched DRX oxyfluoride, $Li_{1.1}Mn_{0.8}Ti_{0.1}O_{1.9}F_{0.1}$. Upon initial cycling, the electrochemical profile of this new DRX material evolves significantly near 4 V and 3 V, leading to a substantial and steady increase in discharge capacity. This early "activation" process is followed by a steady state where the voltage profile stabilizes and the capacity remains nearly constant. Through a detailed analysis of $Li_{1.1}Mn_{0.8}Ti_{0.1}O_{1.9}F_{0.1}$ cathode samples collected at various states of charge by using wide-angle X-ray scattering (WAXS) spectroscopy, solid-state magic angle spinning nuclear magnetic resonance (MAS-NMR), and high-resolution transmission electron microscopy (HRTEM), we elucidate the underlying mechanism that involves the dynamic phase transformation on charge and discharge. The process manifests itself as changes in the local and long-range cation ordering within the rocksalt framework. We further discuss the external and internal driving forces for such cycling-activated changes, including the temperature and voltage window, as well as chemical composition and particle size.

2. Results and Discussion

2.1. Synthesis and properties

The $Li_{1.1}Mn_{0.8}Ti_{0.1}O_{1.9}F_{0.1}$ cathode material was synthesized using a solid-state method, as described in our previous publication.[15] The resulting powder was mixed with carbon black by high-energy ball milling, and is hereafter denoted as M80. Mechanochemical mixing is critical for cathode performance as it reduces particle size and enables intimate carbon mixing with as-

synthesized M80 (denoted as M80_AS), shortening Li diffusion lengths and improving electronic conductivity.[37] The average particle size after ball-milling is in the range of several hundred nanometers, as shown in the scanning electron microscopy (SEM) image (Fig. 1a). A homogeneous distribution of TM cations and O/F anions is observed at the particle level, as confirmed by the energy-dispersive X-ray spectroscopy (EDS) mapping carried out under both SEM (Supplementary Fig. S1a) and high-angle annular dark-field-scanning transmission electron microscopy (HAADF-STEM) (Fig. 1b) imaging modes. A Li : Mn : Ti ratio of 1.098 : 0.810 : 0.092 was determined by inductively coupled plasma mass spectrometry (ICP-MS), close to our target values.

The powder XRD pattern collected on M80 is indexed to a cubic rocksalt structure (S.G. $Fm\bar{3}m$) with a random cation distribution (Fig. 1c). The lattice parameter determined by Rietveld refinement of the XRD pattern is 4.1742 Å. The crystal structure remains unchanged before and after ball milling but notable peak broadening is observed (Supplementary Fig. S1b), consistent with a reduction in crystallite size. The cubic rocksalt structure is also confirmed at a single particle level using selected area electron diffraction (SAED) collected in TEM (Fig. 1d). The *d*-spacings corresponding to the electron diffraction peaks (marked with semicircles) are approximately 2.1 and 1.5 Å, which can be indexed to the (200) and (220) planes of the cubic rocksalt structure, respectively. The SAED pattern also shows broadening of various diffraction spots, and the resulting ring-like features indicate multiple crystallite orientations within a single particle. The square-shaped diffuse scattering patterns (marked with red arrows) are attributed to the presence of short-range order (SRO) in the long-range cation-disordered structure, which has also been reported in previous studies.[38,39] The atomic-resolution crystal structure was examined by HRTEM and the corresponding fast Fourier transform (FFT) patterns are shown in Fig. 1e and f. Small-

angle grain boundaries are observed and are associated with the rotation of the (200) planes (red lines in magnified area in A, Fig. 1e), consistent with the broadening of the SAED diffraction spots (A in Fig. 1f). In addition, the presence of SRO within the cation disordered framework is further confirmed by the square-like diffraction features (B in Fig. 1e and f, respectively). The distribution of both small-angle grain boundaries and SRO are nonuniform, as shown in Supporting Information Fig. S1c,d.

2.2. Electrochemical performance

Fig. 2 shows the electrochemical performance of the M80 cathode when cycled over a voltage window of 1.5–4.8 V at a current density of 10 mA/g. The first cycle has a sloped voltage profile and delivers a discharge capacity of about 160 mAh/g (Fig. 2a). The voltage profile changes rapidly in the second cycle, and this continues through the first 15 cycles, with a flattening of the electrochemical curve near 3.0 V, 3.9 V, and 4.7 V on charge and 3.8 V, 2.9 V and 1.6 V on discharge (Fig. 2b). This is clearly shown by the development of strong peaks in the corresponding differential capacity *vs*. voltage (dQ/dV) plots (Fig. 2c), especially the sharp cathodic peak near 2.9 V, which is not typically observed for Mn-based DRX cathodes with lower Mn content.[34,40] As a result, a much higher discharge capacity of ~ 320 mAh/g is obtained after 30 cycles (Fig. 2a and Supplementary Fig. S2a,b), corresponding to nearly full Li^+ extraction from this compound. Note that the theoretical capacities of M80 are 332 and 242 mA/g based on the Li content and on the Mn^{3+}/Mn^{4+} redox reservoir, respectively. Despite a decrease in the average voltage from 2.92 to 2.79 V (4.5% decrease), a specific energy of ~ 900 Wh/kg is achieved after 30 cycles (Fig. 2d),

corresponding to a 190% increase in energy density in comparison to the initial discharge (Supplementary Fig. S2c-f).

Changes in the voltage profile upon cycling are further examined. Fig. 2e breaks down the charge capacity contributions over the 1.5–3.2 V, 3.2–3.7 V, 3.7–3.95 V, 3.95–4.6 V, and 4.6–4.8 V voltage regions using bars of different colors. Most of the 1st charge capacity is obtained below 4.6 V, with only 15% of the capacity obtained between 4.6 V and 4.8 V and associated with anionic redox.[33,34] The total charge capacity increases rapidly during the initial 15 cycles and stabilizes afterwards (Supplementary Fig. S3a). On 30th charge, the total capacity reaches 345 mAh/g, a 185% increase from the 186 mAh/g obtained on 2nd charge. The additional capacity mostly comes from the 1.5–3.2 V (86 mAh/g, region IV in Fig. 2b,c,e) and 3.7–4.6 V (73 mAh/g, region V in Fig. 2b,c,e) regions. Interestingly, the increase in capacity contribution is much more significant over the former (20% to 36%) than over the latter (39% to 42%) voltage range, indicating that the main contributor to the charge capacity rise is related to the anodic and cathodic processes below 3.2 V. After 15 cycles, there is a noticeable capacity increase over the 3.7–3.95 V region (grey bar in Fig. 2e). On the other hand, the capacity contributions over the 3.2–3.7 V and 4.6–4.8 V voltage ranges decrease from 29% to 13% and from 12% to 9%, respectively.

Upon repeated cycling, the discharge voltage profile also evolves with the following main development (Fig. 2b,c,f): 1) the 3.8 V slope in region I (4.8–3.05 V); 2) an extensive plateau-like feature at 2.9 V in region II (3.05–2.7 V); 3) the 1.6 V slope in region III (2.0–1.5 V). The discharge capacity contributions are calculated in the specific ranges of 4.8–3.5 V, 3.5–3.2 V, 3.2–3.05 V, 3.05–2.84 V, 2.84–2.7 V, 2.7–2.0 V, and 2.0–1.5 V (Fig. 2f). The evolution of the discharge capacity involves activation and growth from cycle 1 to 15, followed by a steady state after cycle 15. In the 30th discharge (Fig. 2f), the capacity contributions over the ranges of 4.8–3.5 V, 3.05–

2.7 V, and 2.0–1.5 V are approximately 20% (64 mAh/g), 39% (122 mAh/g), and 22% (70 mAh/g) of the total capacity (316 mAh/g, Supplementary Fig S3b), corresponding to an increase of 267%, 212%, and 212% compared to the 5^{th} discharge. Here the 5^{th} discharge (instead of the 2^{nd} discharge) was chosen for more accurate comparison. While the biggest capacity change occurs around 3.8 V, most of the discharge capacity is obtained from the plateau-like feature at 2.9 V in region II. A significant capacity loss of 49 mAh/g is observed for the 3.5–3.05 V region, whereas the capacity contribution over the 2.7–2.0 V range stays relatively constant during cycling.

After 30 cycles between 1.5 and 4.8 V, we observed a gradual decrease in the discharge capacity (Supplementary Fig. S2a,b). The capacity retention is largely influenced by the upper and lower cutoff voltages (Supplementary Fig. S2c,d) which also impact the overall evolution of the voltage profile. We note that when the lower cutoff voltage increased to 2.7 V, the voltage profile did not flatten in region II, as shown in Supplementary Fig. S3c. Using an upper cutoff voltage of 4.6 V but the same lower cutoff voltage of 1.5 V, the cell experienced similar trends in voltage and capacity evolution but at a slower rate (Supplementary Fig. S3d-f), resulting in improved cycling stability (Supplementary Fig. S2). In that case, neither capacity decay nor voltage decrease was observed after 30 cycles, suggesting that material's intrinsic structural changes are unlikely to be the source of the performance degradation observed after 30 cycles between 1.5 and 4.8 V. We believe the predominating contributor to capacity decay is the degradation of $LiPF_6$-based electrolyte at the high and/or voltages.[45-46] High-voltage instability of the liquid electrolytes has been extensively reported for cells comprising a traditional layered oxide cathode, although in the case of DRX cathodes, electrolyte stability may be further reduced due to the oxygen redox activities in the active material. Detailed investigation on electrolyte degradation in DRX cells are currently underway.

We note that a faster "activation" of the M80 cathode is enabled by charging and discharging at an elevated temperature. At 50 °C, the initial discharge capacity also increases significantly when cycled at a current density of 100 mA/g (by 185 % as compared to that at 20 °C, Supplementary Fig. S4). Aside from the cycling protocols, several other factors are found to influence the shape of the voltage profile and capacity evolution, particularly Mn content and particle size. Increasing the Mn content is found to induce faster and more drastic changes in both, as shown in Fig. 3a-c that compare the evolution of a previously-reported DRX material $Li_{1.2}Mn_{0.7}Nb_{0.1}O_{1.8}F_{0.2}$ (M70, Mn content = 0.7)[34] and the M80 (Mn content = 0.8) cathode of interest to the present study. The capacity gain for M70 is ~ 120% over 30 cycles, whereas this value increases to ~ 200% for M80. Comparing the dQ/dV plots obtained during the 30th cycle (Fig. 3c), the main redox feature around 2.9 V is also much sharper and stronger in M80. To evaluate particle size effects, M80_AS (with an average particle size of about 10 μm) was ball-milled at a relatively low energy using a speed of 100 rpm, which produce particles in the range of 2-4 μm (denoted as M80_L hereafter). The electrochemical performance of the M80_L cathode was compared to that of the standard M80 cathode formulation involving ball-milling of the M80_AS material at 300 rpm to produce particles in the submicron size range (Fig. 1a). Fig. 3d-f compare the voltage profiles and corresponding dQ/dV plots obtained over the 1.5–4.8 V range at 10 mA/g. Due to slower kinetics in the larger M80_L particles, the 1st cycle discharge capacity of the M80_L cathode is much lower compared to that of the M80 cathode. Both cathodes experience capacity enhancement over the first 30 cycles (Fig. 3d,e), however, the voltage profile evolution over regions II and III is less significant for M80_L (Fig. 3e,f). The overall better performance observed for the M80 cathode composed of smaller-sized particles indicates that particle size reduction enhances kinetics and material utilization. We note that, as the ball milling process also

introduces carbon additives onto the active material particles (as described in the experimental section), electronic conductivity differences in M80_L and M80 likely contributes to the observed performance differences. A detailed understanding of the effects of particle size and conductive additives will be reported in a follow-up publication.

We further evaluated the changes in M80 kinetic properties with cycling. Li chemical diffusion coefficients were determined using potentiostatic intermittent titration technique (PITT) measurements.[41] Compared to the values obtained at the 1st discharge, the Li diffusivity obtained at the 30th discharge is noticeably improved, especially above the open circuit voltage of 3.2 V (Supplementary Fig. S5). The results suggest kinetic improvements at the high-voltage region where most capacity enhancement is observed. We note that the obtained Li chemical diffusion coefficient values may be erroneous as the PITT method is traditionally developed for solid-solution systems.[42,43] The voltage profiles of the activated M80 clearly show plateau-like features, suggesting the existence of pseudo first-order phase transitions.

2.3. Structural evolution of the M80 cathode

To understand the underlying processes resulting in the unique voltage and capacity evolution of the M80 cathode, detailed chemical and structural analyses were performed. The redox activity of the transition metal species during cycling were examined by *ex-situ* hard X-ray absorption spectroscopy (hXAS) on samples collected after various numbers of cycles. Changes in the Mn and Ti valence states were evaluated by comparing the edge energy position, as well as the 1st derivatives of the Mn and Ti *K*-edges X-ray absorption near-edge structure (XANES) spectra, to that of reference compounds.[47] As expected, the average Mn oxidation state is close to

3+ in the pristine M80 cathode (P, Fig. 4a,b and Supplementary Fig. S6b). At the end of the 1st charge to 4.8 V (C1, Fig. 4a and Supplementary Fig. S6a), it is oxidized to 4+ and then returns to 3+ upon subsequent discharge to 1.5 V (D1, Fig. 4b and Supplementary Fig. S6b). Here, we adopt a notation where C and D refer to the 4.8V charged and 1.5 V discharged states, respectively, while the digits indicate the cycle number. The Mn^{3+}/Mn^{4+} redox process is highly reversible throughout cycling, as shown in the XANES spectra collected at C1, C4, and C30 (Fig. 4a and Supplementary Fig. S6a) as well as D1, D15, D22, and D30 (Fig. 4b and Supplementary Fig. S6b,c), where the edge energies vary between similar values on charge and on discharge up to the 30th cycle. The Ti valence state, on the other hand, does not change noticeably on charge and discharge (Supplementary Fig. S6d), indicating that Ti^{4+} does not contribute to the redox processes, consistent with previous reports on similar DRX cathodes.[48] Operando differential electrochemical mass spectroscopy (DEMS) measurements show that oxygen gas evolution was not detected throughout the charge and discharge during the initial cycles (Supplementary Fig. S7). The results suggest that oxygen loss in M80 cathode is minimal.[34,44,45,48,49]

Structural changes during cycling were monitored using *ex-situ* synchrotron WAXS analysis. The technique has an incident beam size of 100 μm^2, which enables the detection of the atomic structure and crystallinity of phases with small crystallite sizes. Compared to the pristine electrode (P), all diffraction peaks for the DRX phase shift towards higher *q* at C1 and then partially reverse back to lower *q* at D1 (Supplementary Fig. S8a), consistent with contraction and expansion of the cubic rocksalt lattice during Li extraction and insertion. Upon further cycling, in the charged state, additional peaks appear near 1.3, 2.5, 3.4, 4.0, and 4.6 $Å^{-1}$ (marked with ◊) while the peaks corresponding to the 111, 200, and 220 reflections of the original DRX phase remain near 2.6, 3.1, and 4.2 $Å^{-1}$ (marked with ♦ and indexed in Fig. 4c). The new peaks are much broader and their

intensities grow with cycling, suggesting the steady growth of a secondary phase with lower crystallinity (or smaller domains) upon cycling. A general shift of the DRX peaks to higher *q* is also observed from C4 to C30 (highlighted by the dashed lines in Fig. 4c), indicating the contraction of the original cubic framework following the integration and growth of the newly formed phase/domains. The structural evolution continues during the discharge process, with significant changes observed at D12 (Fig. 4d and Supplementary Fig. S8b,c). Along with the lower *q* shift (indicated by the dashed lines) of the DRX (200), (220), and (311) peaks, additional peaks (marked with ○) also appear near these reflections, suggesting the formation of a different rocksalt phase at the end of discharge. These new peaks continue to grow throughout cycling, as one can clearly observe them on the D30 sample.

To understand the nature of the structural transformation, we closely examined a series of electrode samples recovered after 30 cycles, after significant evolution of their voltage profiles and capacities. Following from the depth of discharge (DoD) and cutoff voltage used during the 30th discharge, the samples are labeled A (0%, 4.8 V), A' (20%, 3.5 V), B (50%, 2.84 V), B' (65%, 2.7 V), C' (80%, 2.0 V), and C (100%, 1.5 V), as shown in Fig. 5a. In the two-dimensional (2D) WAXS patterns, the pristine electrode P shows the expected cation-disordered α-$LiFeO_2$ rocksalt structure with a random distribution of the Li and TM cations in the O_h sites (Fig. 5b).[50,51] A comparison of the 1D WAXS patterns collected on the A, B, and C samples further highlights the structural changes upon discharge, as shown in Fig. 5c. At the end of charge (sample A), the previously mentioned secondary phase (referred to as the δ phase hereafter) is clearly present. The intensity of the peaks corresponding to the δ phase increases on discharge. By fitting the peaks near 2.5 Å^{-1} (peak 1, δ phase), 2.7 Å^{-1} (peak 2, mainly from DRX (111) reflection), and 3.1 Å^{-1} (peak 3, mainly from DRX (200) reflection) using Gaussian functions, intensity and full width at

half maximum (FWHM) values for each peak can be obtained. The intensity ratio of peak 1 to peak 3, which roughly represents the fraction of δ phase to DRX, is estimated to be 14%, 25%, and 32% for the A, A', and B sample, respectively (Supplementary Fig. S9). The relative increase in the intensity of the δ phase peak, and negligible change to its FWHM, suggest a dominant growth process whereby the size of the δ phase domains increases but the number of those domains does not increase in the material. This is in contrast to a continuous increase in the FWHM of peaks 2 and 3 by 120% at A' and 160% at B, suggesting that the increase in δ phase domain size is accompanied by a decrease in DRX domain size. The results confirm the effective integration of the newly formed δ phase domains within the DRX framework. Although the exact structural characteristics of the δ phase are difficult to ascertain even with the advanced structural probes used in this work, there is evidence for greater cation ordering in the δ phase compared to the pristine DRX phase. For instance, all of the peaks from the δ phase for A match those expected for a spinel-type structure described by the $Fd\bar{3}m$ space group (Fig. 5d top and Supplementary Fig. S10a),[52,53] a result that is consistent with literature examples of phase transformations in Li-Mn-O cathode materials containing predominantly Mn^{4+} with mostly empty Li sites.[21,26,27,54,55] Additional structural information about the δ phase was also obtained from the ^{7}Li NMR studies and will be discussed later.

From A to B' (throughout the voltage regions I and II), the peaks corresponding to the DRX and to the δ phase gradually shift to lower *q*, implying that Li insertion occurs in both phases over this voltage range. As shown in Supplementary Fig. S6e,f and Fig. 2f, considerable Mn reduction occurs in the plateau-like region at B, with its fraction of the total capacity increasing during initial cycling. These results indicate that the transformation to the δ phase and its

integration in the DRX framework is likely the cause of the observed capacity increase with cycling. Upon further Li insertion below 2.7 V (from B' to C), an additional phase transformation is observed. The WAXS pattern of C (marked with ○) matches that of the β'-$LiFeO_2$ structure with monoclinic C2/c symmetry (Fig 5d bottom and Supplementary Fig. S10b),[56-58] a polymorph of α-$LiFeO_2$ disordered rocksalt structure. Previous studies have shown that in β'-$LiFeO_2$, two of the octahedrally coordinated cation sites (Li and Fe) are ordered, whereas the other sites with a distorted tetrahedral coordination are partially ordered,[50,56,59] corresponding to a partially disordered rocksalt (PDRX) structure with a slightly distorted symmetry. The reported XRD pattern of β'-$LiFeO_2$ varies somewhat depending on the synthesis conditions from α-$LiFeO_2$ (Supplementary Fig. S10b).[56,57] We further note that particle size and Li diffusion kinetics are also found to play an important role in the phase transformation. Under the same cycling protocol, both DRX and PDRX phases are detected on the WAXS patterns collected on the discharged M80_L sample obtained after 30 cycles (Supplementary Fig. S11), suggesting incomplete phase transformation at the end of discharge when the sample is composed of larger particles.

Further insights into the structural evolution of the DRX phase and characteristics of the newly-formed phases were obtained from ^{7}Li solid-state NMR. Fig. 5e-g show the ^{7}Li NMR spectra collected on the P, A, A', C', and C samples, respectively, using the pj-MATPASS pulse sequence.[60] In the pj-MATPASS experiment, spinning sidebands due to the fast rotation of the sample during acquisition are effectively removed, resulting in cleaner spectra containing isotropic signals only. For all of the samples, a broad ^{7}Li NMR signal spanning a frequency range from 1000 to −200 ppm is observed, corresponding to Li nuclei in a variety of local environments in the disordered sample. However, the average chemical shift (δ_{avg}) and full width at half maximum (W_{avg}) of the ^{7}Li NMR signals vary significantly between samples. A reliable estimate of the δ_{avg}

value can be obtained by deconvoluting each spectrum using Gaussian components and calculating the barycenter of all of these components by weighing them according to their respective integrated intensities.[61,62] For the pristine M80 sample, a slightly asymmetrical line shape centered around 290 ppm (grey line, top in Fig. 5e) is observed, which are fitted with three Gaussian components (Fig. 5e bottom). We note that this is a simplified model as, in reality, many more distinct Li local environments are present in the disordered structure. A δ_{avg} value of 333 ppm is obtained, along with a broad W_{avg} value of 447 ppm, which is consistent with a highly disordered structure containing Mn^{3+} cations. At the end of charge (sample A), the signal-to-noise ratio is reduced due to the limited amount of Li left in the sample. The most intense ^{7}Li signal is centered around 580 ppm (blue line, Fig. 5f) and is accompanied by a low intensity signal at a lower chemical value of about 109 ppm (purple rectangle, Fig. 5f). While the former can be attributed to ^{7}Li in O_h sites mostly surrounded by nearby Mn^{4+} in the DRX structure, the latter is likely associated with Li in a low coordination environment resulting from local structure changes. Based on a deconvolution of the spectrum collected on sample A using two Gaussian components (Supplementary Fig. S12a), a δ_{avg} value of 521 ppm is obtained. Partial Li^+ re-insertion into the structure, accompanied by partial reduction of Mn^{4+} to Mn^{3+}, leads to the growth of ^{7}Li signal intensity in the 100–400 ppm range in A' (purple rectangle, Fig. 5f). Concurrently, the signal centered at 580 ppm (blue line, Fig. 5f) decreases in relative intensity, which is attributed to a reduced number of Li^+ ions in Mn^{4+}-rich environments. To fit the A' spectrum and mimic the increase in signal intensity in the 100–400 ppm range, two additional Gaussian components centered at 108 and 356 ppm (purple and, magenta signals, Supplementary Fig. S12b) were introduced. This resulting δ_{avg} value is 416 ppm and W_{avg} value is 356 ppm. Based on the WAXS results presented earlier, and given the relatively low resonant frequencies of the new signals in the 100–400 ppm range, we propose that Li^+ inserts

into T_d sites with vacant face-sharing O_h sites over this voltage range.[63] However, the new signals may also arise from Li^+ reinsertion into O_h sites in the DRX framework. A definitive assignment of the NMR data is complicated by the fact that the chemical shift of ^7Li depends not only on its coordination number (O_h *vs.* T_d) and on the nature of neighboring cations, but also on the oxidation state of nearby Mn species (its shift tends to decrease with the average Mn oxidation state). Nonetheless, the presence of well-defined signals at relatively low resonant frequencies (100–400 ppm) for a Mn^{4+}-rich cathode material (A') suggests that the δ phase contains Li in T_d sites and has a more ordered crystal structure than the initial DRX structure, as evidenced by the reduction in W_{avg}.

At a lower voltage (C' sample), where Mn is predominantly in its Mn^{3+} state (Supplementary Fig. S6e,f), the ^7Li spectrum further shifts towards low frequencies and the maximum intensity is observed around 160 ppm (orange line, Fig. 5g). The grey line in Fig. 5g indicates the central frequency observed for the P sample, highlighting the structural differences between the pristine and the cycled sample. The asymmetric line shape of the spectrum collected on the C' sample is attributed to the presence of many overlapping signals resulting from a broad distribution of Li environments in the structure. The signal intensity in the 500–1000 ppm range is consistent with Li in more Mn^{4+}-rich regions, highlighted with a grey rectangle in Fig. 5g (corresponding to the pale orange signal in Supplementary Fig. S12c), almost completely disappears by the end of discharge (C) (Supplementary Fig. S12d), and the overall line shape becomes narrower, in good agreement with the emergence of a partially disordered rocksalt structure. Using three Gaussian components to fit the spectra, the δ_{avg} and W_{avg} values decrease from C' (306 ppm and 336 ppm) to C (260 ppm and 302 ppm). The two major components attributed to the PDRX phase are centered at chemical shift values of 274 ppm and 123 ppm

(orange signals, Supplementary Fig. S12c,d). The peak intensity at 123 ppm slightly increases from C' to C, which is consistent with an increased fraction of Li^+ in T_d sites upon transformation to the β'-$LiFeO_2$ structure. Unlike what was observed for the M70 cathode reported previously, where ^{7}Li NMR spectra span a much broader frequency range with a maximum value of around 500 ppm,[34] the narrowing and reduced shift of the ^{7}Li resonances upon cycling (in the discharged state) reveals structural changes that are unique to high-Mn DRX such as M80.

Atomic-resolution structural analysis was also carried out using HRTEM. SAED patterns collected on single particles of samples A and C no longer show signs of diffuse scattering associated with SRO (Fig. 6a). The *d*-spacings of the ring-like electron diffraction peaks are consistent with those from the WAXS patterns, as shown in the intensity profiles (Fig. 6b). These results confirm that the phase transformation occurs at both the single-particle and bulk sample levels. HRTEM images and corresponding FFT patterns collected on nanoregions of sample C of about 5 nm^2 (labeled 1 to 6) illustrate the various structural features found in neighboring nanodomains (Fig. 6c). Diffraction peaks corresponding to *d*-spacings of 4.8, 2.6, 2.4, 2.2, 2.0 and 1.5 Å are marked with different colors, which correspond to *q* values of 1.3, 2.4, 2.6, 2.8, 3.1 and 4.2 $Å^{-1}$, respectively, in the WAXS profiles shown in Fig. 5c. This suggests a random distribution of crystalline nanodomain orientations in the PDRX phase. Further evidence for this is obtained from the additional HRTEM images at higher magnification, as shown in Supplementary Fig. S13. We believe that the random distribution of crystalline nanodomains has significant implications in the behavior of the M80 cathode, as the domain structure and distribution of nanocrystal orientations influence Li diffusion and structural changes.[64] The observed heterogeneity may relieve some of the strain created by Mn^{3+}-induced Jahn-Teller distortions in individual nanodomains, as has been found in related Li-Mn-O systems.[8,9] We note that for M80, cracking is

not observed after cycling and the particles maintain a uniform elemental distribution, as shown in the STEM-HAADF images and the corresponding EDS maps (Supplementary Fig. S14).

2.4. Discussion

Changes in local cation ordering and coordination, as well as in crystal symmetry, can modify Li^+ ion diffusion pathways, their connectivity, and Li site energies/occupancies in disordered rocksalt cathodes. While it is known that in the DRX structure Li cations diffuse *via* 0-TM channels,[61,65] cation rearrangements and phase transformations can create new Li transport pathways and/or remove existing ones. This is demonstrated here for the M80 DRX cathode, whereby mobile Li and Mn species result in greater cation ordering upon cycling. Additionally, the distribution of cations in the structural framework is dynamic and evolves continuously during charge and discharge. Fig. 7a shows a schematic of the M80 phase evolution. At high voltage, the presence of Mn^{4+} and Li^+ vacancies promotes local cation ordering and a partial transformation of the pristine cubic DRX structure with a random cation ordering (the α phase, Fig. 7b) to a more ordered δ phase, resulting in the integration of the δ domains into the α phase framework. At lower voltages, Mn reduction and Li^+ insertion converts the α and δ phases to a partially disordered rocksalt structure that resembles β'-$LiFeO_2$ with a monoclinic distortion (β' phase, Fig. 7c).[56,58,66] Transformations of the DRX structure to δ and β' are highly correlated with the Li and TM contents in the structure, with the δ phase being TM-rich whereas the β' phase being Li-rich. During the first few charge-discharge cycles (the activation stage), the phase evolution, likely involving Li insertion into T_d sites as well as in the O_h sites, is evidenced by a flattening of the electrochemical curve near 3.0 V, 3.9 V, and 4.7 V on charge and near 3.8 V, 2.9 V and 1.6 V on discharge. These changes continue until the 15^{th} cycle, leading to the development of significant plateau-like

features near 3.8 and 2.9 V on discharge. Afterwards, the evolution reaches a steady state where negligible changes are observed on either voltage profile or total capacity. We believe that, at the steady-state stage, phase transformations occurring during charge and discharge are highly reversible.

We note that the plateau-like features observed for the cycled M80 cathode are different from those typically observed for ordered spinel cathodes, and their notable slopes indicate remaining cation disorder in the material, leading to a distribution of potentials over which Li is extracted from and reinserted into the structure. Aside from their dependence on the chemical composition,[34] the slopes of the plateau-like features are sensitive to Li diffusion in the material and largely influenced by particle size. All in all, the structural evolution of M80, involving Li extraction from/reinsertion into T_d and/or O_h sites and cation ordering in the δ and β' phases, leads to the transformation from a sloped voltage curve typical of a cation-disordered rocksalt (Fig. 7d) to a profile with salient steps at 3.8 and 2.9 V in the partially disordered rocksalt (Fig. 7e). This evolution is not observed for DRX cathodes with a lower Mn content. The structural changes described here indicate a change from a non-topotactic to a pseudo-topotactic Li insertion/extraction mechanism during electrochemical cycling.

As the movement of cations is responsible for the observed structural rearrangements, computational studies that investigate low energy transformation pathways and their synergetic effects in the Mn-rich DRX systems could shed further light on the processes at play here.[67] Nonetheless, the structural transformation mechanism revealed in this study can offer insights into the design of next-generation cathodes with improved structural reversibility for long-term cycling performance. Contrary to the high capacity derived from Li-rich cathode materials that rely on both cationic and anionic redox contributions, the high Mn content in the DRX cathodes such as

M80 enables a larger fraction of capacity obtained from highly reversible transition-metal redox processes. Moreover, the significant role of redox-active transition metal mobility in the phase transformations demonstrated in this study indicate that introducing mobile cations such as those of Cr may lead to further improvements in DRX cathode performance.[48]

We believe the observation made in this study is broadly applicable to Mn-rich DRX materials. **Supplementary Table S1** summarizes previously reported DRX compositions and their cycling behavior. Similar changes in voltage profiles and capacity evolution were observed on DRX materials with either higher Mn or F content,[15,34,40,68-70] although detailed structural analysis was not reported in these studies. This includes studies carried out on $Li_{1.2}Mn_{0.6}Ti_{0.2}O_{1.8}F_{0.2}$,[40] $Li_{1.2}Mn_{0.7}Ti_{0.1}O_2$,[68] $Li_{1.2}Mn_{0.7}Nb_{0.1}O_{1.8}F_{0.2}$,[34] $Li_{1.2}Mn_{0.7}Ti_{0.1}O_{1.7}F_{0.3}$,[69] $Li_{1.1}Mn_{0.8}Ti_{0.1}O_{1.9}F_{0.1}$ (M80, this study), and $Li_{1.05}Mn_{0.9}Nb_{0.05}O_2$.[70] Based on above observations, we estimated a Mn content threshold of about 0.6, above which the structural transformations occur. Given the fact that more extensive phase transformation occurs with increasing Mn content, evidenced by more extensive presence of delta phase in M80 than that in M70, further increasing Mn content beyond 0.8 may lead to better utilization of the phenomena reported in this study. Efforts to stabilize the phase transformation occurring in the Mn-rich partially disordered rocksalt will be an important direction in developing future cathode materials with high energy density.

3. Conclusions

In summary, a submicron-sized Mn-rich disordered rocksalt cathode material was prepared *via* a solid-state synthesis process. During initial electrochemical cycling, the voltage profile evolves significantly near 3.0 V, 3.9 V, and 4.7 V on charge and 3.8 V, 2.9 V and 1.6 V on

discharge, which ultimately leads to the development of plateau-like features and enhancement in the discharge capacity and energy density. These changes are attributed to the structural evolution of the disordered rocksalt during repeated Li extraction/insertion and the accompanying Mn redox. Partial phase transformation to a more ordered structure is observed locally at high voltages, whereas upon extensive Li reinsertion, a partially disordered rocksalt phase forms. After the initial activation and growth stages, the phase transformation is reversible and the detrimental structural degradation is mitigated by the heterogeneous atomic arrangements at the nanoscale. This study provides new structural information and guidance for designing high-performing Mn-based cathode materials for sustainable Li-ion batteries.

4. Methods

4.1. Material synthesis

Stoichiometric amounts of Li_2CO_3 (99.0%, ACS reagent), Mn_2O_3 (99.9%, ACS reagent), TiO_2 (99.0%, anatase ACS reagent), poly(tetrafluoroethylene) (PTFE, mean particle size of 6–9 microns, Goodfellow), and ethanol was mixed *via* a planetary ball milling at 200 rpm for 18 h (PM-100, Retsch). 10% excess Li was used. The precursor mixture was dried and then calcinated at 1050 °C for 12 h under argon (Ar) flow. The heating and cooling rates were set to 5 °C/min. The obtained powder was ground using mortar and pestle in an Ar-filled glove box (O_2 < 1 ppm and H_2O < 1 ppm). The mixture of M70, M80 or M80_L active material with acetylene carbon black (HS-100, Denka) by 8:2 weight ratio was prepared by ball-milling for 12 h at 300 rpm or 100 rpm, respectively.

4.2. Electrochemical evaluation

Electrodes were prepared by casting a slurry mixture of 7:2:1 wt% of the DRX, acetylene black (Denka), and polyvinylidene difluoride (PVDF, kynar flex 2801) binder dissolved in *n*-methyl-2-pyrrolidone (NMP, Sigma-Aldrich) onto an aluminum current collector in an Ar-filled glove box and then dried in a vacuum oven at 120 °C. The 2032-type coin-cell half-cells were assembled with 1 M of lithium hexafluorophosphate ($LiPF_6$) in 1:1 v/v of ethylene carbonate (EC):diethyl carbonate (DEC) (PuriEL, Soulbrain) electrolyte and a polypropylene membrane (PP, Celgard 2500) separator. Lithium foil (Alfa Aesar) was used as counter and reference electrodes. The electrochemical measurements were conducted at a constant current density of 10 mA/g and 100 mA/g in a voltage window between 1.5 V/2.7 V and 4.6 V/4.8 V, at both room temperature (approximately 20 °C) and an elevated temperature of 50°C. All charge and discharge capacities were calculated based on the net active material loading on the electrode. PITT measurements were carried out at room temperature within a voltage window of 2.0 and 4.6 V, using a potential step of 30 mV until the current drops to less than 2 mA/g. The electrochemical data were acquired using a VMP3 battery potentiostat (Bio-Logic science) at room temperature. After cycling, the cathode electrodes were extracted from the coin cells and gently rinsed with dimethyl carbonate (DMC) to remove the residual electrolyte before the analysis.

4.3. Material characterization

SEM and XRD analysis. The SEM images were taken by Field Emission Scanning Electron Microscopy (JEOL 7500F) at 15 kV. Energy-dispersive X-ray spectroscopy maps were collected at 8 kV by using the NSS configuration software. The powder X-ray diffraction was analyzed by

a Bruker D2 powder X-ray diffractometer (Cu Kα, 40 kV, 30 mA, λ = 1.54178 Å). The refinement of the XRD patterns was performed using the Fullprof software.

TEM and STEM analysis. The M80 sample was ultrasonicated in DMC after which the dispersed particles were loaded onto TEM lacey carbon grids in an Ar-filled glovebox. TEM imaging and EDS spectroscopy were conducted on a Titan 80-300™ scanning/transmission electron microscope operated at 300 kV. EDS data were collected using an Oxford X-Max TEM EDS detector. The electron diffraction and FFT patterns were processed using the Digital Micrograph software.

Hard X-ray absorption spectroscopy analysis. XANES spectra were collected using hard XAS at Stanford Synchrotron Radiation Lightsource (SSRL) beamline 2-2 and 4-3. Recovered electrode samples were sealed using polyimide tape and placed at 45° to the incident X-ray beam. The data was processed using the Sam's Interface for XAS Package (SIXPACK[71]) software. For reference, MnO (Mn(II)), Mn_3O_4 (Mn(II/III)),Mn_2O_3 (Mn(III)), and MnO_2 (Mn(IV)) as well as Ti_2O_3 (Ti(III)) and TiO_2 (Ti(IV)) powder standards were used.

Wide angle X-ray scattering analysis. The recovered electrodes were sealed using polyimide tape after the Al substrate was removed. Crystalline phases of the electrode samples were obtained using wide-angle X-ray scattering (WAXS) with a monochromatic X-ray of 0.976254 Å at SSRL beamline 11-3 using 12.7 keV energy. Area diffraction images were collected for a 60 s exposure time and recorded on a 2D Mar345 image plate detector (Marresearch GmbH) with 73.242 × 73.242 μm^2 pixels. Images were calibrated using a LaB6 standard. Transmission geometry was used with a detector distance of 108 mm from the sample. The incident beam on the sample was approximately 100 μm vertical × 100 μm horizontal. To remove the background

interference including the broad peak (at ~ 1.3 $Å^{-1}$) from the polyimide film used to cover the electrode during the analysis, baseline correction was carefully processed in all collected patterns.

Solid-state NMR. Solid state ^{7}Li NMR spectra of the pristine M80 and cycled electrode samples were acquired at B_0 = 2.35 T (100 MHz for ^{1}H) using a wide bore Bruker BioSpin spectrometer equipped with a DMX 500 MHz console and a custom-made 1.3 mm single X-broadband magic angle spinning (MAS) probe tuned to ^{7}Li (38.9 MHz). Each sample was loaded into 1.3 mm zirconia rotors and closed using Vespel™ caps in an Ar-filled glovebox. To avoid air and moisture exposure during data acquisition, the samples were spun using dry nitrogen at the magic angle with υ_R = 60 kHz. ^{7}Li NMR chemical shifts were externally referenced against pure lithium fluoride powder (LiF, $\delta_{iso}(^{7}Li) = -1$ ppm). Isotropic ^{7}Li NMR spectra were recorded using the projected magic angle turning phase-adjusted sideband separation (pj MATPASS) pulse sequence[60,72] which effectively removes spinning sidebands due to MAS. Data were acquired using 90° radiofrequency (RF) pulses of 0.45 μs and signals were averaged over 2000 transients with a recycle delay of 50 ms. This short recycle delay allows ^{7}Li nuclei in Mn-containing phases to be fully relaxed. Solid-state NMR data were processed using the Bruker TopSpin 3.6.0 and spectra were fitted using the DMfit software.[73]

Operando DEMS. The cathodes were made by mixing a slurry of M80 DRX, carbon (acetylene black), and 10 wt.% PVDF (Solef 6010) in NMP (Sigma-Aldrich). The resulting slurry is then spread onto stainless steel mesh and dried under vacuum at 120 °C overnight. For DEMS, hermetically sealed half cells with a cathode and a Li metal anode were assembled in an Ar atmosphere glove box using custom-designed Swagelok-type cells, as described in previous publications.[33] The cells were assembled with a 1 M $LiPF_6$ in 1:1 v/v of EC:DEC electrolyte and a dual layered separator consisting of a microporous monolayer polypropylene membrane (cathode

side, Celgard 2500) and quartz filter paper (anode side, Whatman QMA). The cathode active material loadings were approximately 5 mg/cm^2. The cells were cycled at a constant current of 20 mA/g on a VSP-series potentiostat (Bio-Logic) under positive Ar pressure (≈ 1.2 bar) while any gas evolution was monitored *in situ* using the custom-built DEMS apparatus.[74-76] The cell headspace was sampled every 10 min and any accumulated gases were swept with Ar to the mass spectrometer chamber for analysis.

ASSOCIATED CONTENT

Supporting Information Available: Additional data and figures including XRD and WAXS profiles, SEM, HRTEM, STEM images, EDS elemental mapping, hard XAS spectra, NMR spectra fitting, and electrochemical performance are included.

Acknowledgments

The authors thank Prof. Bryan D. McCloskey and Matthew J. Crafton at UC Berkeley for helping with the DEMS measurements and the related discussions, Drs. Nicholas Strange, Vivek Thampy, Bart A. Johnson, Christopher J. Tassone, Anthony Fong, Charles L. Troxel Jr., and Tim J. Dunn at Stanford Synchrotron Radiation Lightsource for helping with the WAXS measurements and discussion, and Drs. Erik Nelson, Matthew Latimer, and Leah Kelly for helping with the XAS measurements. We appreciate the assistance in ICP measurements from Drs. Daniel Collins-Wildman, Dilni Koggala Wellalage, and Kenneth Higa. Use of the Stanford Synchrotron Radiation Lightsource, SLAC National Accelerator Laboratory, is supported by the U.S. Department of Energy, Office of Science, Office of Basic Energy Sciences under Contract No. DE-AC02-

76SF00515. The TEM work was conducted at the William R. Wiley Environmental Molecular Sciences Laboratory (EMSL), a national scientific user facility sponsored by DOE's Office of Biological and Environmental Research and located at PNNL. PNNL is operated by Battelle for the Department of Energy under Contract DE-AC05-76RLO1830. The NMR results reported here made use of the shared facilities of the UCSB MRSEC (NSF DMR # 1720256), a member of the Material Research Facilities Network (www.mfn.org). V.C.W. was supported by an NSF Graduate Research Fellowship under Grant No. DGE 650114. This work was supported by the Assistant Secretary for Energy Efficiency and Renewable Energy, Office of Vehicle Technologies of the U.S. Department of Energy under Contract No. DE-AC02-05CH11231.

References

1. E. A. Olivetti, G. Ceder, G. G. Gaustad, X. Fu, *Joule* **11**, 229, 2017.

2. M. Greenwood, M. wentker, J. Leker, *Appl. Energy* **302**, 117512, 2021.

3. Electric Vehicle Outlook 2018, Bloomberg New Energy Finance." Bloomberg NEF, 2018, about.bnef.com/electric-vehicle-outlook/#toc-download.

4. M. Wagemaker, F. G. B. Ooms, E. M. Kelder, J. Schoonman, F. M. Mulder, *J. Am. Chem. Soc.* **126**, 13526, 2004.

5. E.-S. Lee, K.-W. Nam, E. Hu, A. Manthiram, *Chem. Mater.* **24**, 3610, 2012.

6. B. Song, G. M. Veith, M. J. Kirkham, J. Liu, J. Park, M. Yoon A. Huq, *Chem. Mater.* **31**, 124, 2019.

7. A. M. Abakumov, S. S. Fedotov, E. V. Antipov, J.-M. Tarascon, *Nat. Commun.* **11**, 4976, 2020.

8. C. Zuo, Z. Hu, R. Qi, J. Liu, Z. Li, J. Lu, C. Dong, K. Yang, W. Huang, C. Chen, Z. Song, S. Song, Y. Yu, J. Zheng, F. Pan, *Adv. Energy Mater.* **10**, 2000363, 2020.

9. X. Zhu, F. Meng, Q. Zhang, L. Xue, H. Zhu, S. Lan, Q. Liu, J. Zhao, Q. Guo, B. Liu, L. Gu, X. Lu, Y. Ren, H. Xia, *Nat. Sustain.* **4**, 392, 2021.

10. T. Sato, K. Sato, W. Zhao, Y. Kajiya, N. Yabuuchi, *J. Mater. Chem. A* **6**, 13943, 2018.

11. Y. Zhang, A. Hu, J. Liu, Z. Xu, L. Mu, S. Sainio, D. Nordlund, L. Li, C.-J. Sun, X. Xiao, Y. Liu, F. Li, *Adv. Funct. Mater.* **32**, 2110502, 2022.

12. V. V. Kosilov, A.V. Potapenko, S. A. Kirillov, *J. Solid State Electrochem.* **21**, 3269, 2017.

13. A. Manthiram, K. Chemelewski, E.-S. Lee, *Energy Environ. Sci.* **7**, 1339, 2014.

14. J. Lee, C. Wang, R. Malik, Y. Dong, Y. Huang, D.-H. Seo, J. Li, *Adv. Energy Mater.* **11**, 2100204, 2021.

15. J. Ahn, D. Chen, G. Chen, *Adv. Energy Mater.* **10**, 2101671, 2020.

16. W. Hua, S. Wang, M. Knapp, S. J. Leake, A. Senyshyn, C. Richter, M. Yavuz, J. R. Binder, C. P. Grey, H. Ehrenberg, S. Indris, B. Schwarz, *Nat. Commun.* **10**, 5365, 2019.

17. J. Zheng, P. Xu, M. Gu, J. Xiao, B. D Browning, P. Yan, C. Wang, J-G. Zhang, *Chem. Mater.* **27**, 1381, 2015.

18. P. K. Nayak, D. Boopathi, E. Levi, J. Grinblat, Y. Elias, B. Markovsky, D. Aurbach, *ACS Appl. Energy. Mater.* **5**, 4279, 2022.

19. T. Liu, J. Liu, L. Li, L. Yu, J. Diao, T. Zhou, S. Li, A. Dai, W. Zhao, S. Xu, Y. Ren, L. Wang, T. Wu, R. Qi, Y. Xiao, J. Zheng, W. Cha, R. Harder, I. Robinson, J. Wen, J. Lu, F. Pan, K. Amine, *Nature* **606**, 305, 2022.

20. N. J. Dudney, J. B. Bates, R. A. Zuhr, S. Young, J. D. Robertson, H. P. Jun, S. A Hackney, *J. Electrochem. Soc.* **146**, 2455, 1999.

21. R. J. Gummow, D. C. Liles, M. M. Thackeray, *Mat. Res. Bull.* **28**, 1249, 1993.

22. M. M. Thackeray, *Prog. Solid St. Chem.* **25**, 1, 1997.

23. N. Mosquera, F. Bedoya-Lora, V. Vasquez, F. Vasquez, J. Calderon, *J. Appl. Electrochem.* **51**, 1419, 2021.

24. B. Shi, J. Gim, L. Li, C. Wang, A. Vu, J. R. Croy, M. M. Thackeray, E. Lee, *Chem. Commun.* **57**, 11009, 2021.

25. Y. Liu, G. Liu, H. Xu, Y. Zheng, Y. Huang, S. Li, J. Li, *Chem. Commun.* **55**, 8118, 2019.

26. Y. I. Jang, B. Huang, H. Wang, D. R. Sadoway, Y.-M. Chiang, *J. Electrochem. Soc.* **146**, 3217, 1999.

27. A. R. Armstrong, N. Dupre, A. J. Paterson, C. P. Grey, P. G. Bruce, *Chem. Mater.* **16**, 3106, 2014.

28. T. Uyama, K. Mukai, I. Yamada, *RSC Adv.* **8**, 26325, 2018.

29. J. M. Paulsen, C. L. Thomas, J. R. Dahn, *J. Electrochem. Soc.* **146**, 3560, 1999.

30. X. Wen, B. Qiu, H. Gao, X. Li, Z. Shi, Z. Liu, *ACS Appl. Energy Mater.* **5**, 9079, 2022.

31. Z. Cai, H. Ji, Y. Ha, J. Liu, D.-H. Kwon, Y. Zhang, A. Urban, E. E Foley, R. Giovine, H. Kim, Z. Lun, T.-Y. Huang, G. Zeng, Y. Chen, J. Wang, B. D. McCloskey, M. Balasubramanian, R. J. Clément, W. Yang, G. Ceder, *Matter* **4**, 12, 2021.

32. H. Ji, K. Wu, Z. Cai, J. Liu, D.-H. Kwon, H. Kim, A. Urban, J. K. Papp, E. Foley, Y. Tian, M. Balasubramaniam, H. Kim, R. J. Clement, B. D. McCloskey, W. Yang, G. Ceder, *Nat. Energy* **5**, 213, 2020.

33. M. J. Crafton, Y. Yue, T.-Y. Huang, W. Tong, B. D. McCloskey, *Adv. Energy Mater.* **10**, 2001500, 2020.

34. J. Ahn, Y. Ha, R. Satish, R. Giovine, L. Li, J. Liu, C. Wang, R. J. Clement, R. Kostecki, W. Yang, G. Chen, *Adv. Energy Mater.* **12**, 2200426, 2022.

35. M. Freire, N. V. Kosova, C. Jordy, D. Chateigner, O. I. Lebedev, A. Maignan, V. Pralong, *Nat. Mater.* **15**, 173, 2016.

36. M. Freire, O. I. Lebedev, A. Maignan, C. Jordy, V. Pralong, *J. Mater. Chem. A* **5**, 21898, 2017.

37. M. Park, X. Zhang, M. Chung, G. B. Less, A. M. Sastry, *J. Power Sources* **195**, 7904, 2010.

38. H. Ji, A. Urban, D. A. Kitchaev, D.-H. Kwon, N. Artrith, C. Ophus, W. Huang, Z. Cai, T. Shi, J. C. Kim, H. Kim, C. Ceder, *Nat. Commun.* **5**, 592, 2019.

39. K. V. Mishchenko, M. A. Kirsanova, A. B. Slobodyuk, A. A. Krinitsyna, N. V. Kosova, *Chimica, Techno Acta*, **9**, 20229310, 2022.

40. L. Li, Z. Lun, D. Chen, Y. Yue, W. Tong, G. Chen, G. Ceder, C. Wang, *Adv. Funct. Mater.* **31**, 2101888, 2021.

41. C. J. Wen, B. A. Boukamp, R. A. Huggins, *J. Electrochim. Acta* **126**, 2258, 1979.

42. Y. Zhu, C. Wang, *J. Phys. Chem. C* **114**, 2830, 2010.

43. B. C. Han, A. V. Ven, D. Morgan, G. Ceder, *Electochim. Acta* **29**, 4691, 2004.

44. M. B. Yahia, J. Vergnet, M. Saubanere, M.-L. Doublet, *Nat. Mater.* **18**, 496, 2019.

45. K. McColl, R. A. House, G. J. Rees, A. G. Squires, S. W. Coles, P. G. Bruce, B. J. Morgan, M. S. Islam, *Nat. Commun.* **13**, 5275, 2022.

46 M. Liu, J. Vatamanu, X. Chen, L. Xing, K. Xu, W. Li, *ACS Energy Lett.* **6**, 2096, 2021.

47. T. Liu, A. Dai, J. Lu, Y. Yuan, Y Xiao, L. Yu, M. Li, J. Gim, L. Ma, J. Liu, C. Zhan, L. Li, J. Zheng, Y. Ren, T. Wu, R. Shahbazian-Yassar, J. Wen, F. Pan, K. Amine, *Nat Commun.* **10**, 4721, 2019.

48. J. Huang, P. Zhong, Y. Ha, D.-H. Kwon, M. J. Crafton, Y. Tian, M. Balasubramanian, B. D. McCloskey, W. Yang, G. Ceder, *Nat. Energy* **6**, 706, 2021.

49. Q. Jacquet, A. Iadecola, M. Saubanere, H. Li, E. J. Berg, G. Rousse, J. Cabana, M.-L. Doublet, J.-M. Tarascon, *J. Am. Chem. Soc.* **141**, 11452, 2019.

50. J. C. Anderson, M. Schieber, *J. Phys. Chem. Solids* **25**, 961, 1964.

51 G. C. Mather, C. Dussarrat, J. Etourneau, A. R. West, *J. Mater. Chem.* **10**, 2219, 2000.

52. A. Jain, S. P. Oug, G. Hautier, W. chen, W. D. Richards, S. Dacek, S. Dacek, S. Cholia, D. Gunter, D. Skinner, G. Ceder, K. A. Persoon, *APL Materials* **1**, 011002, 2013.

53. D. A. Kitchaev, S. T. Dacek, W. Sun, G. Ceder, *J. Am. Chem. Soc.* **139**, 2672, 2017.

54. M. M. Thackeray, A de Kock, *Mat. Res. Bull.* **28**, 1041, 1993.

55. C. Fong, B. J. Kennedy, *Z. Kristallogr. Krist.* **209**, 941, 1994.

56. M. Barre, M. Catti, *J. Solid Stat. Chem.* **182**, 2549, 2009.

57. M. Tabuchi, K. Ado, H. Sakaebe, C. Masquelier, H. Kageyama, O. Nakamura, *Solid State Ionics* **79**, 220, 1995.

58. M. Tabuchi, S. Tsutsui, C. Masquelier, R. Kanno, K. Ado, I. Matsubara, S. Nasu, H. Kageyama, *J. Solid Stat. Chem.* **140**, 159, 1998.

59. A. Meyer, M. Catti, R. Dovesi, *J. Phys. Condens. Matter* **22**, 146008, 2010.

60. I. Hung, L. Zhou, F. Pourpoint, C. P. Grey, Z. Gan, *J. Am. Chem. Soc.* **134**, 1898, 2012.

61. R. J. Clement, Z. Lun, G. Ceder, *Energy Environ. Sci.* **13**, 345, 2020.

62. F. Geng, B. Hu, C. Li, C. Zhao, O. Lafon, J. Trebosc, J.-P. Amoureux, M. Shen, B. Hu, *J. Mater. Chem. A* **8**, 16515, 2020.

63. A. Abdellahi, A. Urban, S. Dacek, G. Ceder, *Chem. Mater.* **28**, 5373, 2016.

64. W. Chen, X. Zhan, R. Yuan, S. Pidaparthy, A. X. B. Yong, H. An, Z. Tang, K. Yin, A Patra, H Jeong, C. Zhang, K. Ta, Z. W. Riedel, R. M. Stephens, D P. Shoemaker, H. Yang, A. A. Gewirth, P. V. Braun, E. Ertekin, J.-M. Zuo, Q. Chen, *Nat. Mater*. 2022.

65. J. Lee, A. Urban, X. Li, D. Su, G. Hautier, G. Ceder, Science 343, 519, 2014.

66. Pierre Villars (Chief Editor), PAULING FILE in: Inorganic Solid Phases, SpringerMaterials (online database), Springer, Heidelberg (ed.).

67. I. D. Seymour, S. Chakraborty, D. S. Middlemiss, D. J. Wales, C. P. Grey, *Chem. Mater.* **27**, 5550, 2015.

68. K. Zhou, Y. Li, S. Zheng, M. Zhang, C. Zhang, C. Battaglia, H. Liu, K. Wang, P. Yan, J. Liu, Y. Yang, *Energy Storage Mater.* **43**, 275, 2021.

69. S. Patil, D. Darbar, E. C. self, T. Malkowski, V. C. Wu, R. Giovine, N. J. Szymanski, R. D. McAuliffe, B. Jiang, J. K. Keum, K. P. Koirala, B. Ouyang, K. Page, C. Wang, G. Ceder, R. J. Clement, J. Nanda, *Adv. Energy Mater.* 223207, 2022.

70. J. Lee, C. Wang, R. Malik, Y. Dong, Y. Huang, D.-H. Seo, J. Li, *Adv. Energy Mater.* **11**, 2100204, 2021.

71. Webb S.M., SIXPACK: A graphical user interface for XAS analysis using IFEFFIT. *Physica Scripta* T115, 1011, 2005.

72. Z. Gan, R. R. Ernst, *J. Magn. Reson. Series A* **123**, 140, 1996.

73. D. Massiot, F. Fayon, M. Capron, I. King, S. L. Calve, B. Alonso, J.-O. Durand, B. Bujoli, Z. Gan, G. Hoatson, *Magn. Reson. Chem.* **40**, 70, 2002.

74. B. D. McCloskey, A. Valery, A. C. Luntz, S. R. Gowda, G. M. Wallraff, J. M. Garcia, T. Mori, L. E. Krupp, J. Phys. *Chem. Lett.* **4**, 2989, 2013.

75. B. D. McCloskey, D. S. Bethune, R. M. Shelby, G. Girishkumar, A. C. Luntz, *J. Phys. Chem. Lett.* **2**, 1161, 2011.

76. B. D. McCloskey, A. Speidel, R. Scheffler, D. C. Miller, V. Viswanathan, J. S. Hummelshøj, J. K. Nørskov, A. C. Luntz, *J. Phys. Chem. Lett.* **3**, 997, 2012.

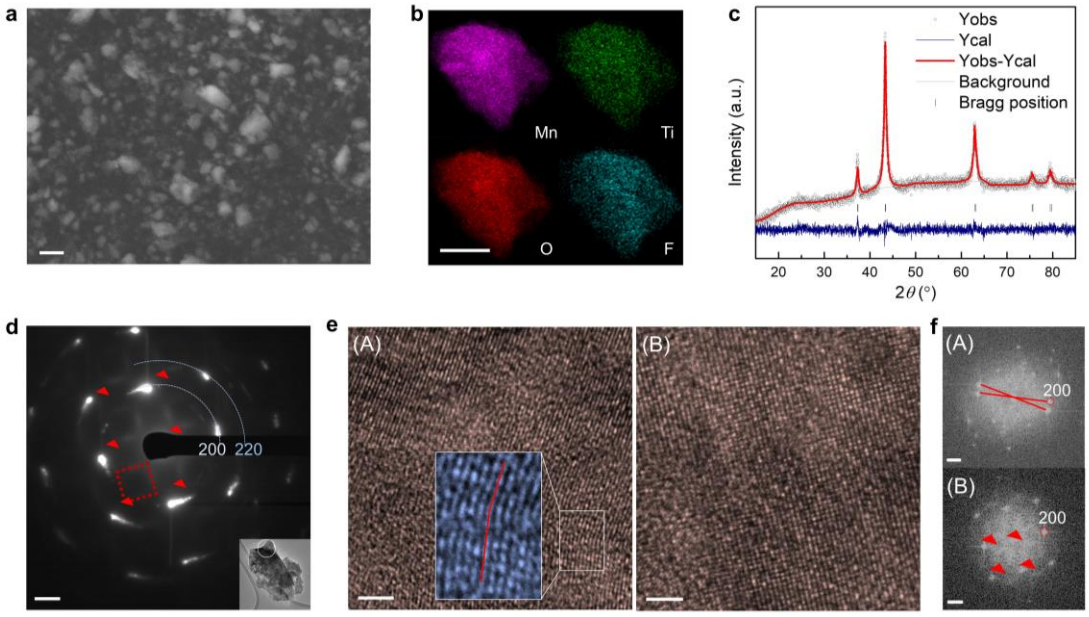

Figure 1. Material characterization of M80. **a**. SEM image of the M80 powder. Scale bar is 1 μm. **b**. STEM-HAADF EDS elemental maps of a single particle. Mn (magenta), Ti (green), O (red), and F (cyan). Scale bar is 100 nm. **c**. Refinement result of the XRD pattern collected on the M80 powder, which corresponds to the cation-disordered cubic rocksalt structure with $Fm\bar{3}m$ symmetry. **d**. SAED pattern obtained from the part of a single particle (inset image). Scale bar is 2 nm^{-1}. The semicircles are assigned to the (200) and (220) planes of the DRX, while the red square and arrows indicate SRO. **e**. HRTEM images collected on different areas of a particle labeled (A) and (B). Scale bars are 2 nm. The red line in the magnified area (A) highlights small-angle grain boundaries. **f**. FFT patterns obtained from regions (A) and (B) in (**e**). Scale bars are 2 nm^{-1}. The red lines in (A) indicate the rotation of the crystal planes while the red arrows in (B) are attributed to the presence of SRO.

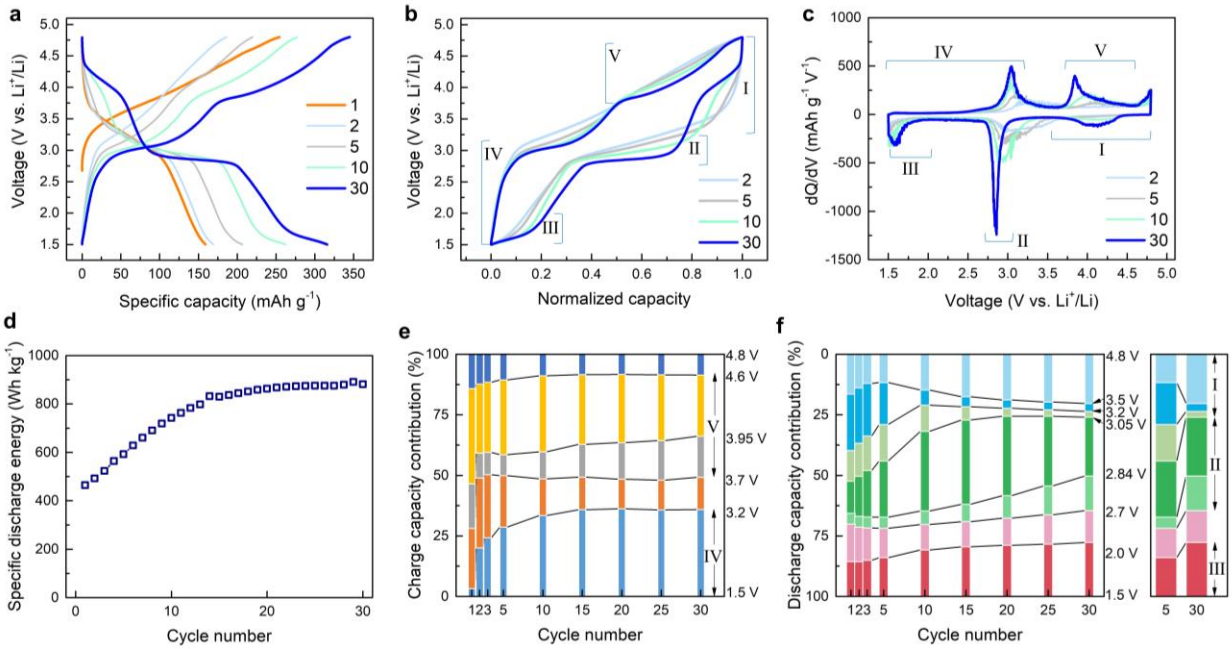

Figure 2. Electrochemical performance of the M80 cathode. **a**. Charge and discharge voltage profiles for the 1st (orange), 2nd (light blue), 5th (grey), 10th (green), and 30th (blue) cycles operated in the voltage range of 1.5–4.8 V at a current density of 10 mA g^{-1}. **b**. Voltage profiles plotted as a function of the normalized capacity. The discharge voltage regions are labeled I (4.8–3.05 V), II (3.05–2.7 V), and III (2.0–1.5 V) while the charge voltage regions are labeled IV (1.5–3.2 V) and V (3.7–4.6 V). Those labels are used to describe the voltage evolution and capacity rise. **c**. Corresponding differential capacity *vs*. voltage (*d*Q/*d*V) curves. **d**. Specific discharge energy during the initial 30 cycles. **e**,**f**. Specific charge and discharge capacity contributions over various voltage ranges for select cycles between 1 and 30. In (**e**), the blue, orange, grey, yellow, and dark blue bars correspond to the following charge voltage ranges: 1.5–3.2 V, 3.2–3.7 V, 3.7–3.95 V, 3.95–4.6 V, and 4.6–4.8 V, respectively. In the 1st cycle, the blue bar is counted from the open circuit voltage. In (**f**), the pale blue, blue, light green, green, pale green, pink, and red bars correspond to the following discharge voltage ranges: 4.8–3.5 V, 3.5–3.2 V, 3.2–3.05 V, 3.05–2.84 V, 2.84–2.7 V, 2.7–2.0 V, and 2.0–1.5 V, respectively. The 5th and 30th discharges are compared on the right.

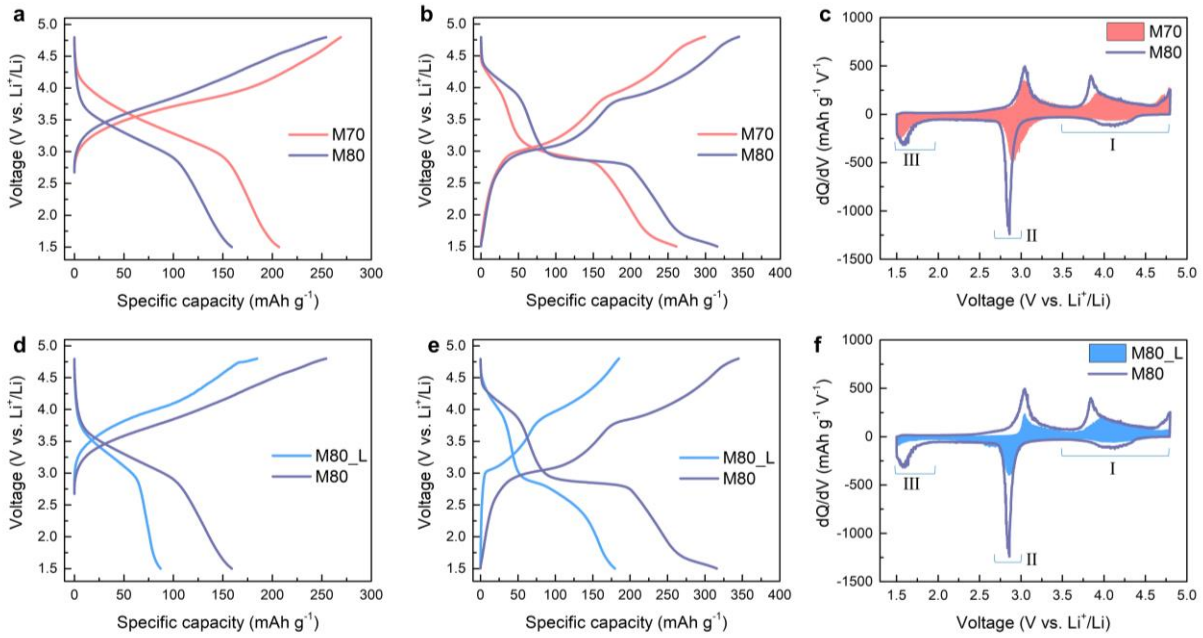

Figure 3. Effects of chemical composition and particle size on the electrochemistry. a-c. Comparison of the electrochemical performance of the M80 (purple) and M70 (pink) cathodes. (**a**) the 1st charge-discharge voltage profiles, (**b,c**) the 30th charge-discharge voltage profiles and corresponding *d*Q/*d*V plots. **d-f**. Comparison of the electrochemical performance of the M80 (purple) and M80_L (blue) cathodes. (**d**) the 1st charge-discharge voltage profiles, (**e,f**) the 30th charge-discharge voltage profiles and corresponding *d*Q/*d*V plots. The cells were tested over the voltage range of 1.5–4.8 V at a current density of 10 mA g^{-1}.

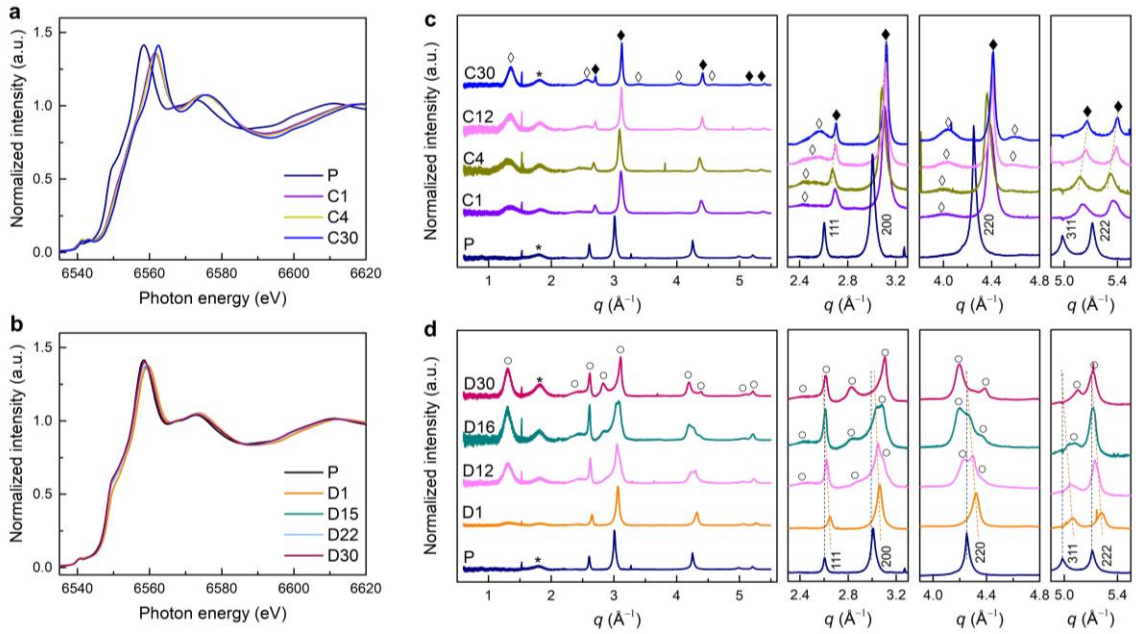

Figure 4. **Redox processes and phase evolution upon cycling of M80 cathode**. **a,b**. Normalized Mn *K*-edge XANES spectra collected on the pristine (P) cathode and on electrodes recovered at the end of (**a**) charge and (**b**) discharge. In the legend, C and D refer to the charged state at 4.8 V and discharged state at 1.5 V, respectively, while the digits indicate the cycle number. **c**,**d**. Normalized WAXS profiles collected on the pristine cathode and on cathode samples recovered at the end of (**c**) charge and (**d**) discharge. The sharp peaks near *q* values of 1.5, 3.2, 3.8, and 5.2 $Å^{-1}$ are attributed to background artifacts. The broad feature near 1.8 $Å^{-1}$ (marked with *) includes the peak from the carbon. In (**c**), the appearance of new peaks near 1.3, 1.8, 2.5, 3.4, 4.0 and 4.6 $Å^{-1}$ (marked with ◊) indicates the formation of a second phase, besides the DRX phase (marked with ♦). For the P sample, each DRX peak is labeled according to its corresponding 111, 200, 220, 311, and 222 reflections. The green dashed line highlights the shift of the peaks going from C4 to C30. In (**d**), the new peaks (marked with ○) indicate the transformation of the DRX phase to a new rocksalt phase. The orange dashed line indicate lower *q* shift from the peak positions of the D1 sample with cycling. The blue dashed lines indicate the peak positions for the P sample. The cells were cycled over the 1.5–4.8 V range at 10 mA g^{-1}.

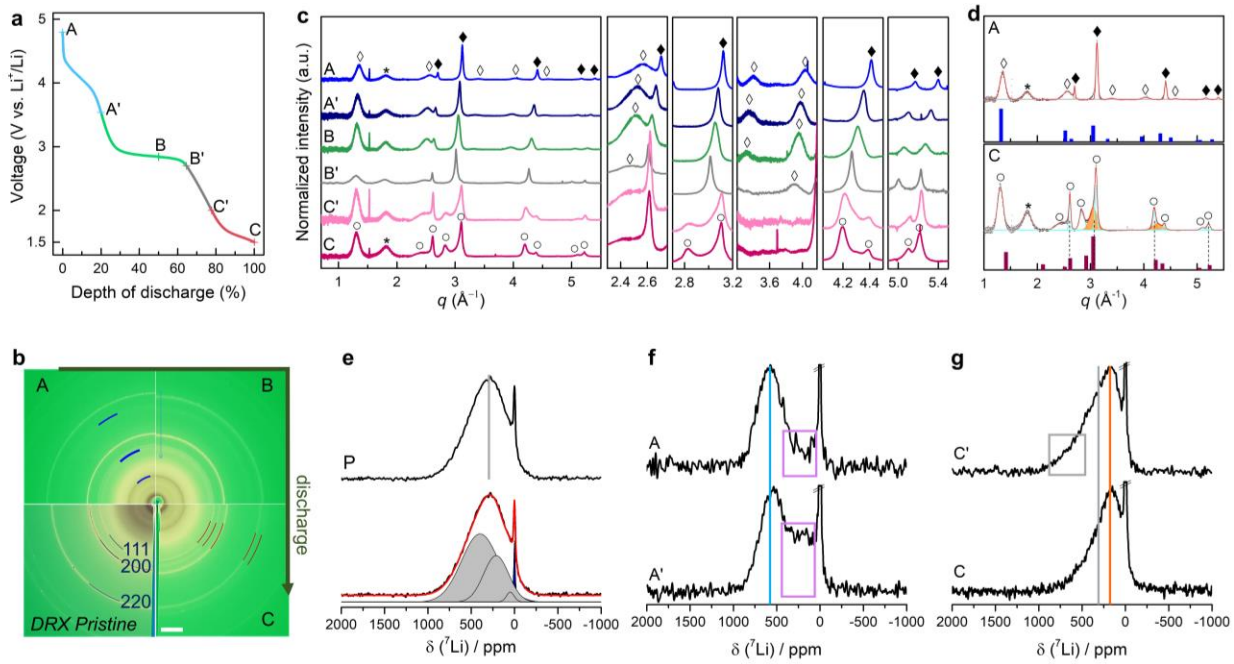

Figure 5. Structural transformation of M80. a. Discharge voltage profile obtained during the 30th cycle and plotted as a function of the depth of discharge (DoD). The recovered electrode samples were obtained at A (0% DoD, 4.8 V), A' (20%, 3.5 V), B (50%, 2.84 V), B' (65%, 2.7 V), C' (80%, 2.0 V), and C (100%, 1.5 V). **b**. 2D WAXS patterns for the pristine (P) and recovered electrodes at the end of charge (A), in the middle of the discharge process (B), and at the end of discharge (C) during the 30th cycle. **c**. Normalized WAXS profiles collected on the recovered electrodes at various DoD and cutoff voltages marked in (**a**). Magnified profiles are shown on the right where the peaks attributed to the δ (◊ and ♦), DRX (♦), and PDRX (○) phases are marked accordingly. The broad feature near 1.8 Å^{-1} (marked with *) includes the peak from carbon. The sharp peaks near 3.7, 4.0, and 5.2 Å^{-1} are attributed to background artifacts. **d**. Experimental WAXS profile (black circles) and fitted spectra (red line) using Gaussian functions obtained on the sample A (top) and C (bottom). (top) Simulated XRD pattern of a λ-MnO_2 with a cubic $Fd\bar{3}m$ space group (mp-25275)[52,53] is shown in blue. (bottom) Estimated XRD pattern of the β'-$LiFeO_2$ with a monoclinic $C2/c$ space group is shown in red bars. The dominant sharp peaks are aligned to the reference peaks (dashed lines). The broad peaks (shaded areas in orange) are attributed to the DRX phase. The reference β'-$LiFeO_2$ sample was prepared by annealing α-$LiFeO_2$ at 400 °C for 150 h.[56] **e**-**g**. ^{7}Li solid-state NMR isotropic spectra collected on the (**e**) P, (**f**) A and A', (**g**) C' and C samples using the pj-MATPASS pulse sequence[60]. In **e**, deconvolution of ^{7}Li fully isotropic pj-MATPASS spectrum (in black) for the P sample using 3 Gaussian components (grey signals).

A Lorentzian component was used to account for the Li-based diamagnetic impurities (dark blue signal). The lines indicate chemical shift values of 290 ppm (grey line), 580 ppm (blue line), and 160 ppm (orange line) shown in **e**, **f**, and **g**, respectively. The sharp peak around 0 ppm is attributed to diamagnetic Li environments formed during electrode preparation and electrochemical cycling (*e.g.*, due to residual Li-containing precursor phases or to electrolyte degradation).

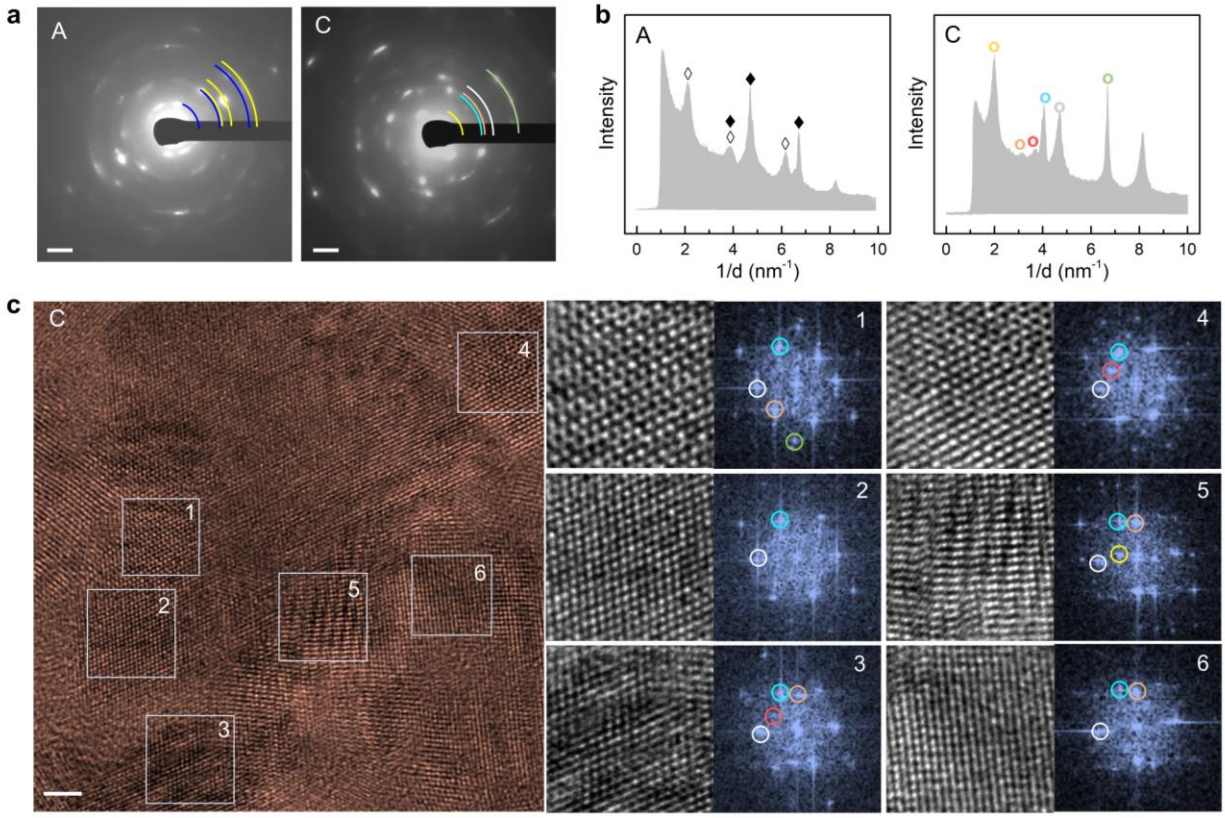

Figure 6. Nanodomain structure in the cycled M80. a,b. SAED patterns and corresponding intensity profiles, respectively, obtained from a single particle sample at the end of charge (A) and end of discharge (C) during the 30th cycle. In (**a**), scale bars are 2 nm^{-1}. For sample A, the blue and yellow semicircles correspond to the *d*-spacings marked with ◊ and ♦ in (**b**), respectively. For sample C, the semicircles highlighted in different colors correspond to the peaks labeled with similar colors in (**b**). **c**. HRTEM image obtained on the discharged sample C. Scale bar is 2 nm. Magnified images and FFT patterns collected on different areas of the particle are displayed on the right. The *d*-spacings marked in yellow, peach, red, blue, white, and green are approximately equal to 4.8, 2.6, 2.4, 2.2, 2.0, and 1.5 Å, respectively, consistent with those shown in the intensity profile in **b**.

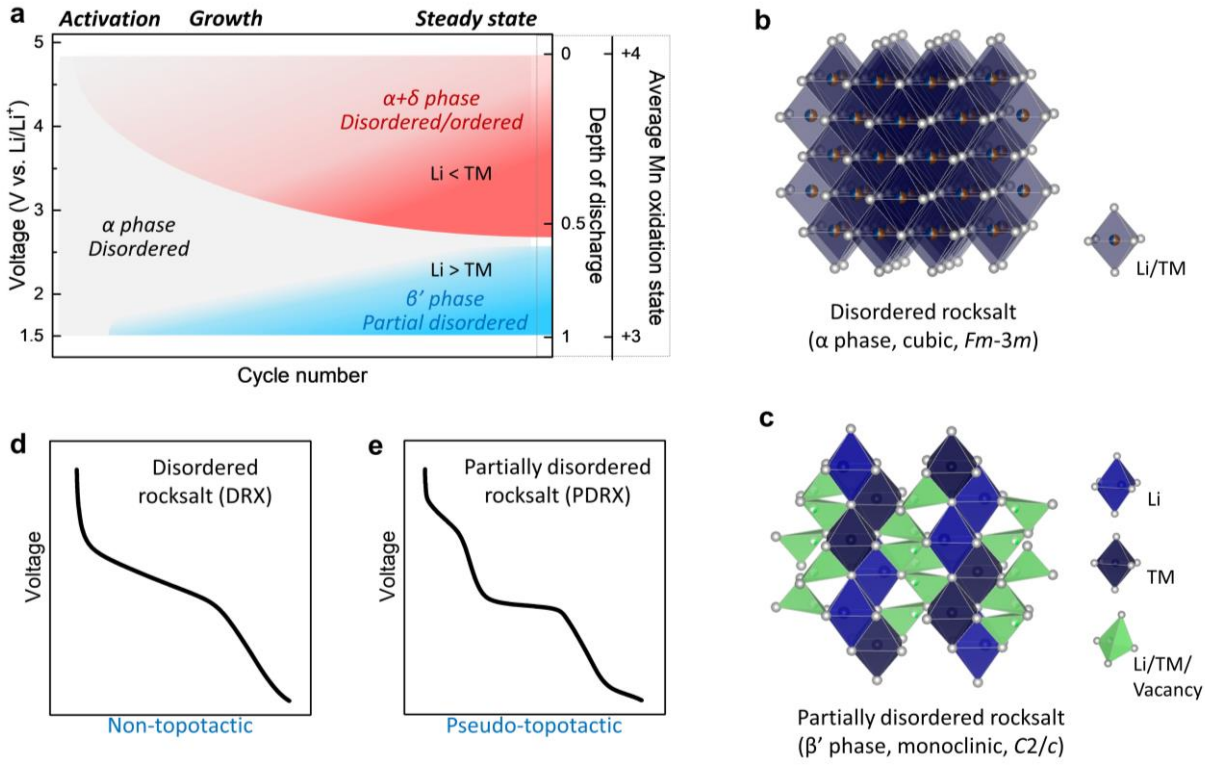

Figure 7. **Schematics of the proposed structural evolution in Mn-rich DRX (M80) cathode.** **a**. Proposed phase map during electrochemical cycling of the M80 DRX cathode. The grey, red, and blue areas correspond to regions where the α, δ, and β' phases described in the main text dominate, respectively. At the steady state, the DoD (Li concentration) and average Mn oxidation state are estimated. **b**. Crystal structure of the fully disordered rocksalt with a cubic $Fm\bar{3}m$ space group. Li and TM cations (shown in navy) randomly occupy the octahedral sites. **c**. Crystal structure of the partially disordered rocksalt structure with a monoclinic $C2/c$ space group.[56,66] Li and TM cations occupying octahedral sites are shown in blue and dark blue, respectively, whereas Li and TM cations randomly occupying tetrahedral sites are shown in green. **d**,**e**. Discharge voltage profiles obtained from (**d**) the initial DRX structure and (**e**) the transformed PDRX structure. The former shows the sloped curve corresponding to a non-topotactic Li insertion/extraction process while the latter exhibits the plateau-like slope that corresponds to a pseudo-topotactic reaction process.